Supporting Information:

Synchronized redox pairs in metal oxide/hydroxide chemical analogues for efficient oxygen evolution reaction

Table S1. OER activity comparison with previously reported $CoMn_2O_4$-based electrocatalysts.

| Electrocatalyst	Synthesis route	Electrolyte concentration (KOH)	Potential mV @ 10 mA/cm^2 (vs RHE)	Tafel slope (mV dec)	Ref.
$CoMn_2O_4$/$CoMn(OH)_x$	**Electrodeposition**	**1M**	**260**	**29**	**This work**
10S-$CoMn_2O_4$/FTO	Electrodeposition	0.1M	300	26.28	[1]
$CoMn_2O_4$ nanodots/rGO	Hot injection & Heating up method	0.1M	310	56	[2]
Mn_3O_4@$CoMn_2O_4$-Co_xO_y	One-pot two-step method	0.1M	310	81	[3]
$Mn_xCo_{3-x}O_4$ Spinel oxides	Sol-gel method	1M	327	79	[4]
$CoMn_2O_4$/N doped porous carbon	Solvothermal	0.1M	570	Not mentioned	[5]

The table represented above shows all the previously reported $CoMn_2O_4$-based catalysts with their overpotential at $10mA/cm^2$ and Tafel slope values. The table shows that this work supersedes both the results in terms of overpotential and kinetics.

1. Procedure of electrodeposition:

Before electrodeposition, Ni-foam was carefully cleaned with concentrated HCL (36 wt. %) in an ultrasonic bath for 5 minutes to remove the NiO layer on the surface followed by rinsing with deionized water and absolute ethanol.

The electrodeposition has been done using potassium chloride (KCl) (99.5%, Merck), $CoCl_2.6H_2O$ (98%, Sigma-Aldrich), $MnCl_2.4H_2O$ (≥98% Sigma Aldrich), Ni-foam (HI-TECH Scientific Equipment). In a typical synthesis 0.01M $CoCl_2.6H_2O$, 0.02M $MnCl_2.4H_2O$, and 0.1M KCl (supporting electrolyte) were dissolved in 50mL of deionized water and kept under stirring for 15 minutes at room temperature. For the process, a three-electrode cell has been used that consists of pre-cleaned Ni-foam (1 x 0.3) cm^2 as the working electrode, Pt wire as the counter electrode, and Ag/AgCl (saturated KCl) as the reference electrode. A potentiostatic electrodeposition was carried out at -1.1V (vs. Ag/AgCl) for 10s at 92^0C over a hot plate to get the desired compound.

2. FTIR analysis:
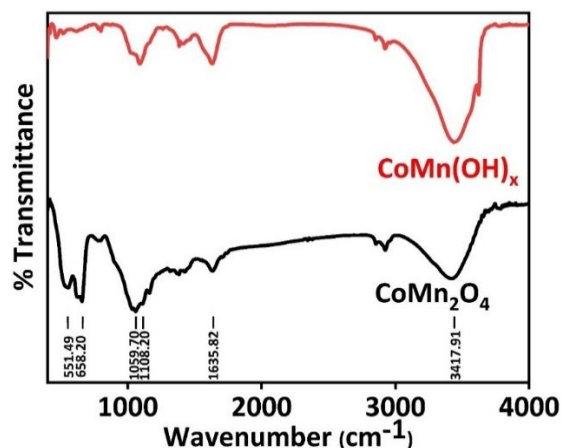
Figure S1: FTIR spectra of synthesized $CoMn_2O_4$ and $CoMn(OH)_x$ substrate.

FTIR spectra displayed absorption bands around 3700 -2690 and 1635 cm^{-1}, attributed to the stretching vibrations of -OH and the bending vibrations of H-O-H from water molecules on the surface and this is consistent with the published data.[1] Importantly, the characteristic peak above 551.49 cm^{-1} and at 1108.82 cm^{-1} confirm the spinel structure of the product.

3. Raman analysis:
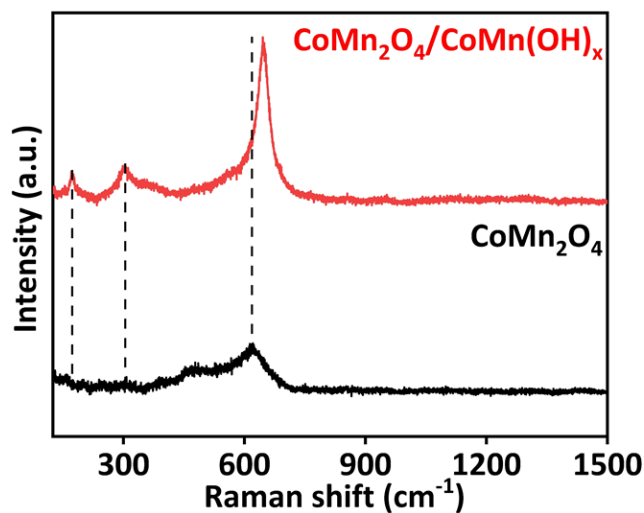
Figure S2: Raman spectroscopy of bare $CoMn_2O_4$ and composite $CoMn_2O_4/CoMn(OH)_x$

Raman spectroscopy was performed to understand the electronic interactions among the components, as shown in the figure above instance peak at 620 cm^{-1} corresponds to E_g vibrational mode of $CoMn_2O_4$. After the formation of the composite, the shift toward higher frequency represents the successful formation of the heterostructure. Additional peaks at 175cm^{-1} and 305cm^{-1} were observed, which corresponds to the vibrational mode from $CoMn(OH)_x$ layer.

4. FESEM images for the composite:

To confirm the formation of the overlayer in the composite, we have synthesized the bare CMO over Ni-foam as mentioned in the synthetic procedure, then intentionally covered half of the CMO with the CMOH overlayer so that we can observe the borderline between bare CMO and CMOH distinctively in the FESEM images. The images shown below (figure S3(a)) show the two distinct layers of CMO and CMOH deposited over Ni-foam. Figure S3(b) shows a schematic representation of the two layers.
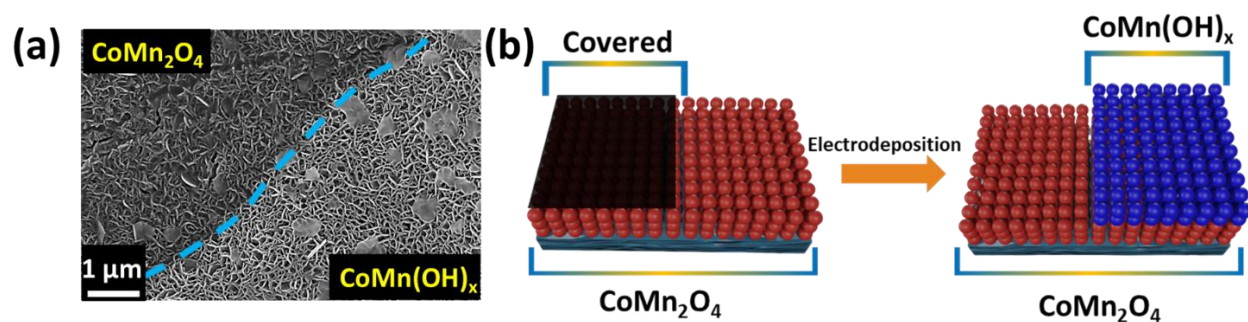
Figure S3: (a) FESEM image for CMO/CMOH composite (b) schematic representation of the two-layer synthesis for FESEM imaging

5. TEM images and EDS analysis:

To confirm the formation of CMOH overlayer, and homogeneous distribution of all the elements over the composite on a nanometer scale FETEM images and FETEM-EDS analysis has been performed.
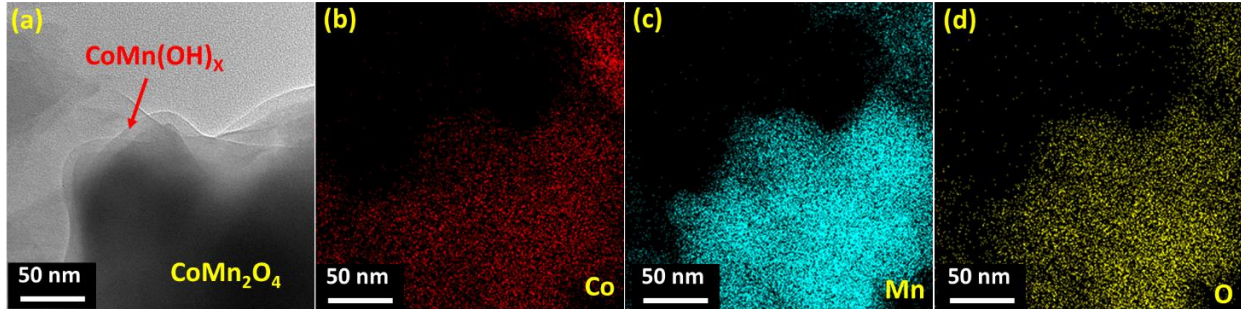
Figure S4: (a) FETEM image of the CMO/CMOH composite (b-d) FETEM-EDS elemental mapping for the CMO/CMOH composite, showing the homogeneous distribution of all the elements

6. X-ray photoelectron spectroscopy analysis:
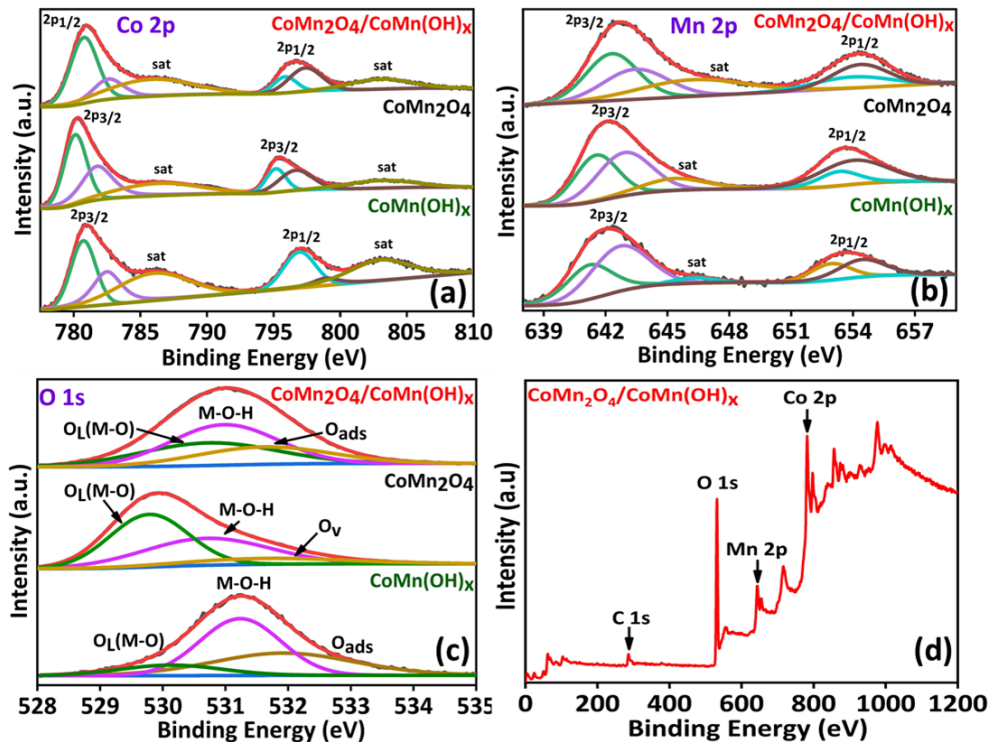
Figure S5: XPS core level spectra, (a) Mn 2p and (b) Co 2p of bare CMOH, CMO, and CMO/CMOH composite (c) O 1s of CMOH, CMO, and CMO/CMOH (d) XPS survey spectra of CMO/CMOH

For the investigation of change in the electronic structure environments around the elements and chemical composition, X-ray photoelectron spectroscopy (XPS) measurements were carried out. The survey spectra shown in figure S5(d) confirms the presence of all the elements in the CMO/CMOH composite. Figure 5(a) and 5(b) show the Mn 2p and Co 2p core level spectra of bare CMOH, CMO, and CMO/CMOH composite. In bare CMO, de-convoluted peaks at 641.57 eV and 643.02 eV correspond to $2p_{3/2}$, and peaks at 653.38eV and 654.11eV correspond to $2p_{1/2}$ of Mn atom, again for Co atom the $2p_{3/2}$ peaks appear at 780.19 eV and 781.81 eV whereas $2p_{1/2}$ peaks are at 795.20 eV and 796.77 eV respectively. Peaks at the binding energy of 786.40 eV, 803.08, and 645.20 eV are assigned to the satellite peaks of Co and Mn respectively for bare CMO. For composite CMO/CMOH, de-convoluted peaks at 642.33 eV and 643.53 eV correspond to $2p_{3/2}$, 654.18 eV and 654.46 eV associated with $2p_{1/2}$ of Mn atom, similarly 780.89 eV and 782.68 eV peaks are assigned to $2p_{3/2}$, and peaks at 795.89 eV and 797.55 eV correspond to $2p_{1/2}$ of Co atom. Binding energy peaks at 786.25 eV, 802.98 eV, and 646.88 eV are the satellite signatures that correspond to the Co and Mn atom of the CMO/CMOH composite respectively. From the acquired XPS data it has been observed that there is a shift in the peak positions towards the higher binding energy in the composite material than that of the bare CMO, indicating a good electronic interaction between the CMO and CMOH. By comparing bare CMOH and CMO/CMOH composite, we observe the same change in binding energy towards a higher value for composite indicating a lower electron density at the surface causing more efficient OER kinetics. Figure S4

(c) shows the O 1s core level spectra of bare CMOH, CMO, and its composite CMO/CMOH. For the composite, the peaks at the binding energy of 530.70 eV, 531.01 eV, and 531.82 eV corresponds to lattice oxygen (O_L) metal hydroxyl group (M-O-H) and adsorbed oxygen (O_{ads}). For the bare counterpart we observe peak associated with lattice oxygen (O_L) at 529.79 eV, metal hydroxide group (M-O-H) at 530.71 eV, and oxygen vacancies (O_V) at 531.62 eV for CMO. In case of bare CMOH peaks at binding energies 529.92 eV, 531.22eV, and 532.01eV corresponds to O_L, M-O-H, and O_{ads} respectively.

7. Conversion of Hg/HgO potentials to RHE:

In all the electrochemical measurements the applied potentials vs Hg/HgO were represented in terms of reversible hydrogen electrode (RHE). The conversion formula for applied potential from Hg/HgO to RHE can be represented as:

$$E_{RHE} = E_{Hg/HgO} + 0.059pH + E^{\circ}_{Hg/HgO} \dots\dots\dots\dots\dots\dots\dots\dots\dots\dots\dots\dots\dots(1)$$

Whereas E_{RHE} and $E^{\circ}_{Hg/HgO}$ are the potential against RHE and reference Hg/HgO electrode, respectively.

8. Optimization of electrodeposition time of CoMn₂O₄ for best OER performance:

To measure the electrodeposition time at which the working electrode shows its best result (OER) is determined by electrodepositing CMO at different time scales as shown in the figure S6, from the figure it is observed that 10 seconds of electrodeposition gives the best value of overpotential 360mV @10mA/cm^2.
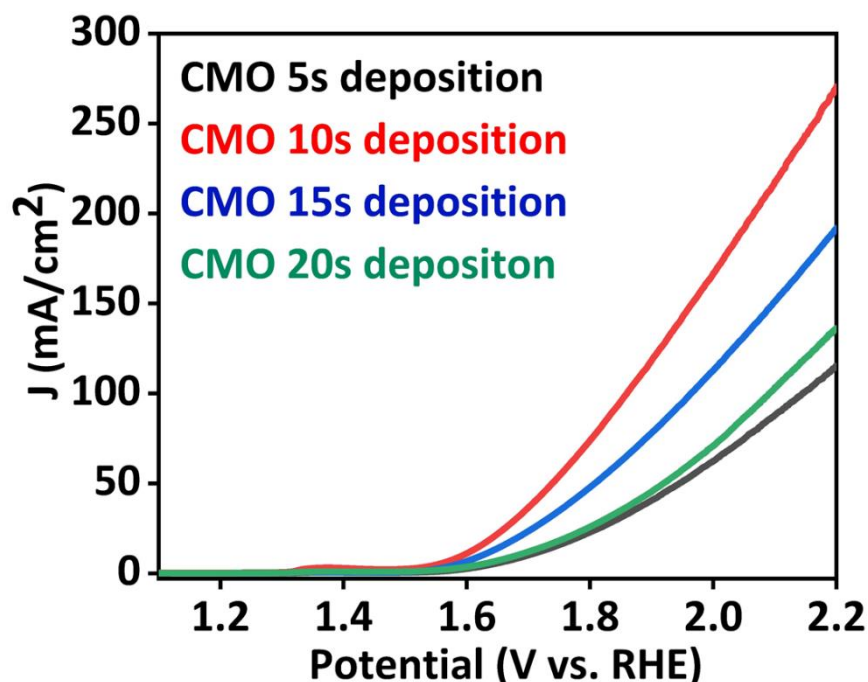
**Figure S6:** Electrodeposition time optimization curve for $CoMn_2O_4$ to get the best result

9. Electrocatalytic activity surface area (ECSA) estimation:

To determine the electrochemical surface area (ECSA), which is indicative of the number of electrochemically active sites in an electrocatalyst, cyclic voltammetry measurements of CMO and CMO/CMOH electrodes were done (shown in figure S7) in the range of -0.08 - 0.04 V vs Hg/HgO (non-Faradic region) at different scan rates of 1-10 mV/sec. Double layer capacitance (C_{dl}), which gives a direct estimate of ECSA value, was calculated from the plot of the difference in current density (j_{anode} - $j_{cathode}$ at 0.95V vs RHE) of CMO/CMOH and CMO electrodes against the scan rate, where C_{dl} is equal to half of the obtained slope value.

ECSA is proportional to the C_{dl} value as follows,

$$ECSA = C_{dl}/C_s \dots\dots\dots\dots\dots\dots\dots\dots\dots\dots\dots\dots\dots\dots\dots\dots\dots\dots(2)$$

To calculate the ECSA value, we have to determine the C_s (specific capacitance of the material) value by synthesizing an atomically smooth planar surface, which is not practical. But it has been found that for alkaline medium (NaOH), the C_s value for all the materials varies in the range of 0.022–0.130 mF/cm^2, and in general, the average C_s value considered is 0.040 mF/cm^2
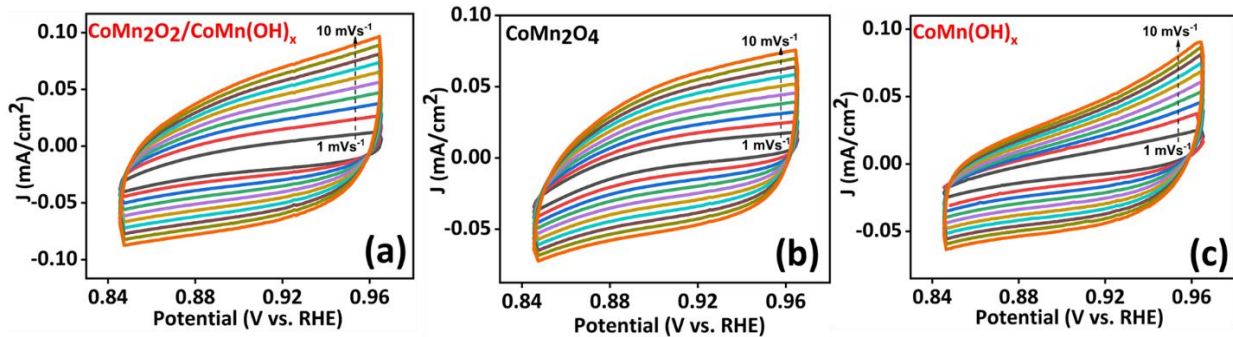
Figure S7: Cyclic voltammetry plots at different scan rates under alkaline conditions in a three-electrode electrochemical cell in a non-faradaic region of the respective catalysts (a) Bare CMO, (b) MCO/CMOH composite.

10. Turnover frequency (TOF):

The TOF value is calculated using the following equation,

$$\text{TOF}= \frac{J \times A}{4 \times F \times \text{Ns}} \dots\dots\dots\dots\dots\dots\dots\dots\dots\dots\dots\dots\dots\dots\dots\dots\dots\dots\dots(3)$$

where J, A, F, and NS are, respectively, the current density at a certain overpotential (A/cm^2), the surface area of the working electrode (cm^2), Faraday constant (96458 C/mol), and concentration of active sites in the catalysts (mol/cm^2). NS for oxygen evolution reaction (OER) was determined by CV measurements at different scan rates in the voltage range where redox reaction occurs. The peak current is plotted against the scan rate where the slope has the linear relationship,

$$Slope = n^2F^2AN_s/4RT\dots\dots\dots\dots\dots\dots\dots\dots\dots\dots\dots\dots\dots\dots\dots(4)$$

in which n, R, and T are the number of electrons transferred, ideal gas constant, and absolute temperature [6–8].

11. Stability:

Cyclic voltammogram in figure S8 (a, b) shows stability test till 1000 cycles of CV measurement for CMO and CMO/CMOH respectively, at the scan rate of 10 mV/sec in the region (0.90 – 1.50 V vs RHE). Figure S8 (c, d) shows the current density of the CMO/CMOH composite, and the bare CMO measured before and after 1000 cycles of CV displays an insignificant change in current density, confirming the stability of both electrodes.
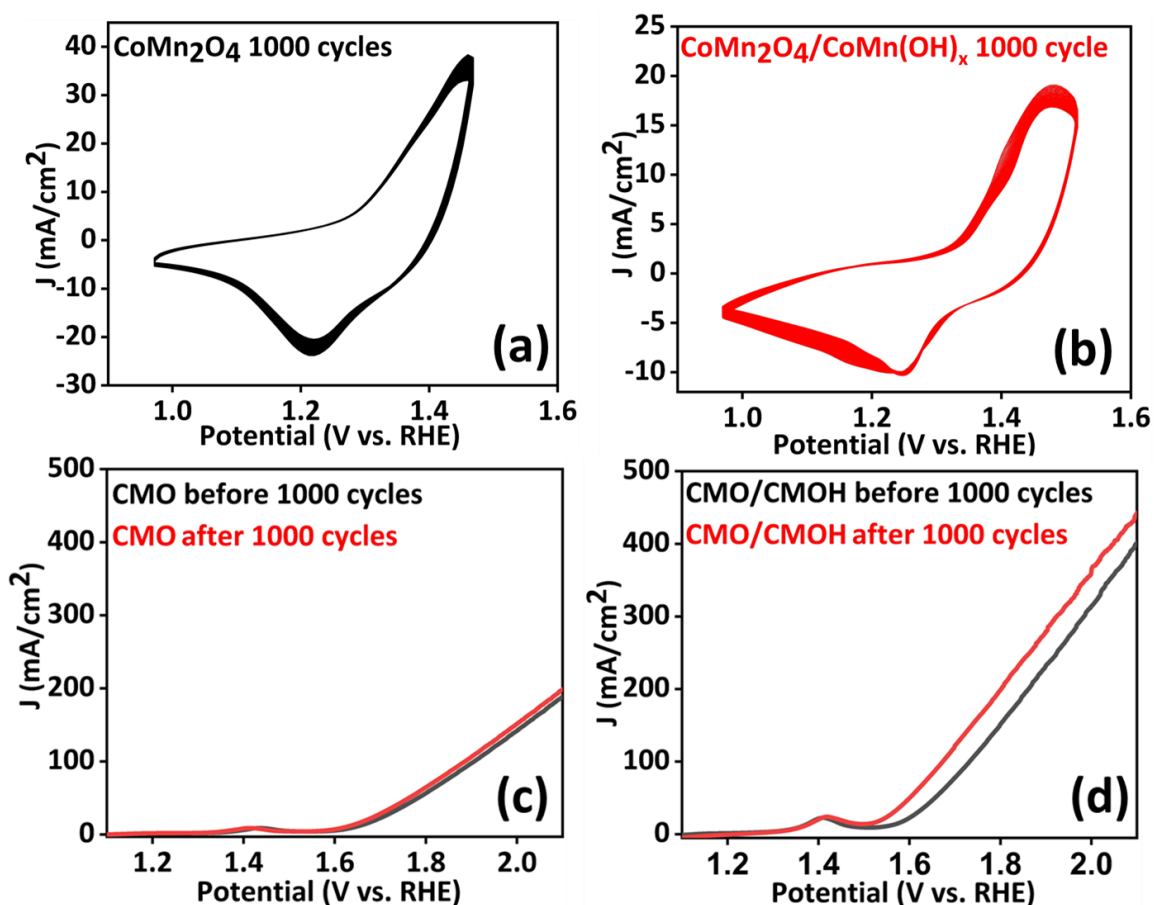

Figure S8: To check the stability of the $CoMn_2O_4/CoMn(OH)_x$ catalyst and its bare counterpart. (a, b) 1000 cycles of cyclic voltammetry of $CoMn_2O_4$ and $CoMn_2O_4/CoMn(OH)_x$ respectively at the scene rate of 10 mV/sec in the region 0.90V to 1.50V vs RHE, (c, d) Current density of the

bare $CoMn_2O_4$ and $CoMn_2O_4/CoMn(OH)_x$ composite measured before and after the long term stability test that shows no such decrease in current density confirming the stability of both the electrodes.

## 12. Characterizations after stability measurements:

12.a. X-ray diffraction analysis
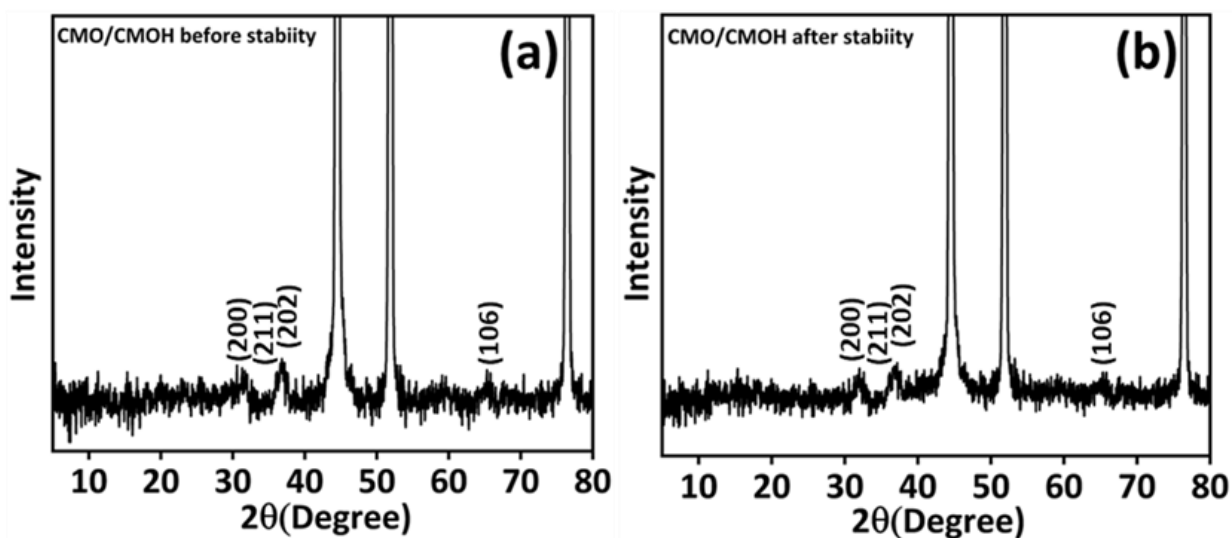
**Figure S9:** (a,b) XRD pattern for CMO/CMOH before and after stability

From the above X-ray diffraction pattern, it is clear that the phase purity of the catalyst has been intact throughout the process.

12.b. Comparison of X-ray photoelectron spectroscopy (XPS) analysis before and after the electrochemical measurements:
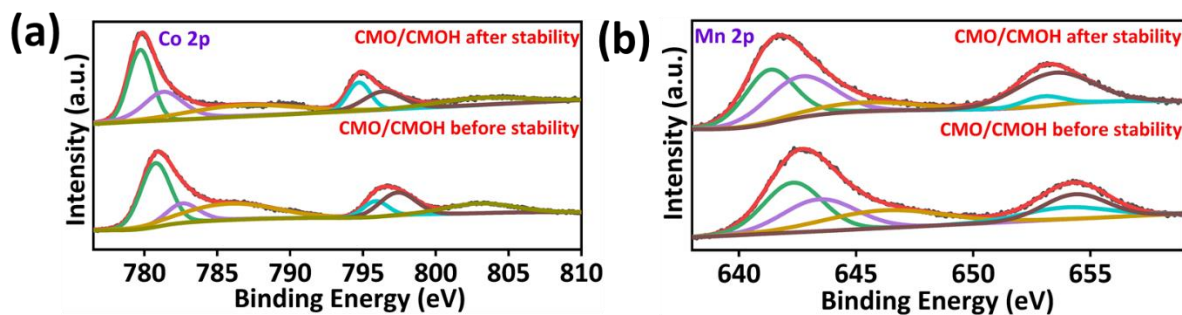
Figure S10: (a,b) X-ray photoelectron spectroscopy data for Co 2p, and Mn 2p before and after the stability test

13. ECSA-normalized OER
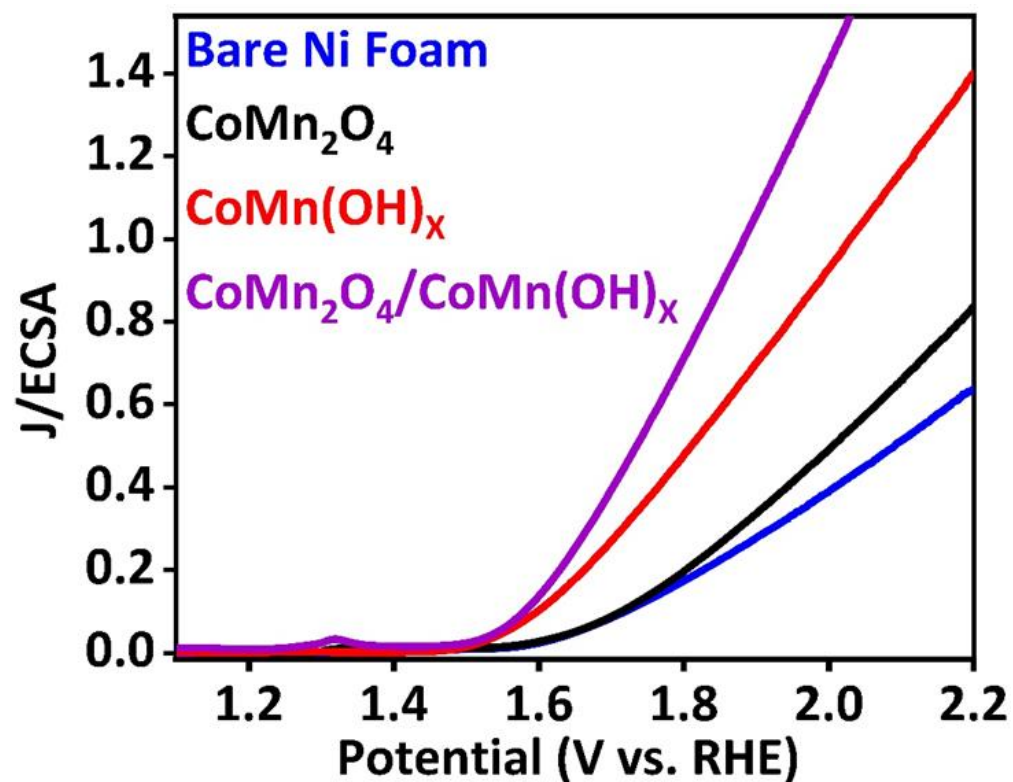
Figure S11: ECSA-normalized OER activity curve

To calculate the ECSA-normalized OER activity, we have normalized the OER polarization curve with respect to the ECSA value of composite CMO/CMOH (325 cm^2)

References:

1   A. Bahadur, W. Hussain, S. Iqbal, F. Ullah, M. Shoaib, G. Liu and K. Feng, *J. Mater. Chem. A*, 2021, **9**, 12255–12264.

2   J. Du, C. Chen, F. Cheng and J. Chen, *Inorg. Chem.*, 2015, **54**, 5467–5474.

3   Z. Luo, E. Irtem, M. Ibánez, R. Nafria, S. MartÍ-Sánchez, A. Genç, M. de La Mata, Y. Liu, D. Cadavid, J. Llorca, J. Arbiol, T. Andreu, J. R. Morante and A. Cabot, *ACS Appl. Mater. Interfaces*, 2016, **8**, 17435–17444.

4   K. Lankauf, K. Cysewska, J. Karczewski, A. Mielewczyk-Gryń, K. Górnicka, G. Cempura, M. Chen, P. Jasiński and S. Molin, *Int. J. Hydrogen Energy*, 2020, **45**, 14867–14879.

5   J. L. Digol, M. F. M. Labata, M. F. Divinagracia and J. D. Ocon, *ECS Trans*, 2017, **77**, 525–531.

6   M. W. Louie and A. T. Bell, *J. Am. Chem. Soc.*, 2013, **135**, 12329–12337.

7   M. Gong, Y. Li, H. Wang, Y. Liang, J. Z. Wu, J. Zhou, J. Wang, T. Regier, F. Wei and H. Dai, *J. Am. Chem. Soc.*, 2013, **135**, 8452–8455.

8   H. Han, H. Choi, S. Mhin, Y. R. Hong, K. M. Kim, J. Kwon, G. Ali, K. Y. Chung, M. Je, H. N. Umh, D. H. Lim, K. Davey, S. Z. Qiao, U. Paik and T. Song, *Energy Environ. Sci.*, 2019, **12**, 2443–2454.